

Modelling and validation of dielectric properties of human skin in the MHz region focusing on skin layer morphology and material composition

Sonja Huclova¹, Daniel Erni² and Jürg Fröhlich¹

¹ Laboratory for Electromagnetic Fields and Microwave Electronics, ETH Zurich, Gloriastrasse 35, 8092 Zurich, Switzerland

² General and Theoretical Electrical Engineering (ATE), Faculty of Engineering, University of Duisburg-Essen, and CeNIDE - Center for Nanointegration Duisburg-Essen, D-47048 Duisburg, Germany

E-mail: j.froehlich@ifh.ee.ethz.ch

Received 18 June 2011, in final form 14 November 2011

Published 16 December 2011

Online at stacks.iop.org/JPhysD/45/025301

Abstract

Human skin consists of several layers with distinct dielectric properties. Physiological processes leading to changes in dielectric properties of the specific layers can potentially be non-invasively monitored employing dielectric spectroscopy. So far no comprehensive skin and underlying tissue model is available for this purpose in the frequency range between 1 and 100 MHz. Focusing on this dispersion-dominated frequency region, different multilayer skin models are investigated. First, with sublayers obtained from two-phase mixtures, second, three-phase mixtures of shelled cell-like ellipsoids and finally, multiphase mixtures obtained from numerical models of single cells generated using a flexible surface parametrization method. All models are numerically evaluated using the finite-element method and a fringing field sensor on the top of the multilayer system serving as a probe. Furthermore, measurements with the sensor probing skin *in vivo* were performed. The validity of the models was tested by removing the uppermost skin layer, the stratum corneum (SC). It was found that only a three-phase mixture (extracellular medium, cell membrane and cytoplasm) at least can qualitatively reproduce the measured dispersion still occurring without the SC if the model is set up without *a priori* knowledge of the dispersive behaviour as e.g. a Cole–Cole fit to measured data. Consequently, microstructural features of tissue have to be part of any accurate skin model in the MHz region.

(Some figures may appear in colour only in the online journal)

1. Introduction

In clinical practice there is a trend towards non-invasive diagnosis, mainly in order to reduce the infection risk and enabling continuous monitoring but also to increase patient comfort. Dielectric spectroscopy and electric impedance spectroscopy is already used for inspection of cervical squamous tissue since the cell shape is subsequently modified with advancing precancerous stage [1], skin cancer [2],

skin irritations [3], ischemia detection [4], measurement of oedema in irritant-exposed skin [5], monitoring of *in vitro* tissue engineering [6] or tumour characterization [7]. On the microscopic scale specific techniques based on dielectric spectroscopy such as impedance flow cytometry, dielectrophoresis and electrorotation [8–13] are employed for the investigation of single cells.

A particular application seeming to be feasible is the analysis of blood parameters through monitoring variations

of dielectric properties caused by physiological changes [14]. However, these measurements face similar challenges as experienced when applying electrodes on the skin in other medical applications such as EEG, EMG, etc. The skin itself is a lossy, layered tissue, whereby the sublayers possess very distinct material compositions and therefore distinct dielectric properties. In addition to the skin structure itself the electrode–skin interface as well as other variations affect dielectric measurements. Facing the mentioned issues numerical modelling turns out to become increasingly challenging. In order to be able to extract any desired parameters from measured data a very accurate solution of the forward problem is indispensable.

To date no comprehensive (continuous) set of the dielectric properties of skin layers stratum corneum (SC), epidermis, dermis and hypodermis is available in the frequency range between 1 and 100 MHz. In [15, 16] the dielectric properties of the uppermost layer, the SC, have been assessed by *in vivo* measurements of skin with and without this top layer. Coaxial probes of different sizes were employed in order to distinguish the SC, epidermis/dermis and hypodermis (subcutaneous fat), providing permittivity estimations for these layers, however, only at single frequencies [16]. Powdered native SC was also measured with a coaxial probe using the time domain reflectometry (TDR) method by [17] including an identification and quantification of two relaxation processes in the microwave frequency range. *In vivo* skin measurements as well as measurements of blood, infiltrated and non-infiltrated fat were performed in [18], also providing Cole–Cole relaxation models for all measured materials. In [19] human skin was measured *in vivo*, also including a Cole–Cole fit. As observed in [20] the Cole–Cole fits are a popular and useful tool in order to describe dielectric spectra of tissue in general. However, an unambiguous physical and physiological interpretation of the obtained Cole–Cole parameters remains difficult, because the impact of the numerous morphological and dielectric parameters as well as their variations has only partially been assessed so far.

Alternative modelling methods of other tissues or tissue-like structures using mixing formulae in the context of the effective medium approach or numerical methods have been presented e.g. in [1, 21], or [22]. The modelling procedure in this work is a combination of those methods including a multiscale approach introduced in [23, 24].

Depending on the probe geometry, effective dielectric parameters of layered structures such as skin are usually a combination of the dielectric properties of the sublayers. In order to obtain the dielectric behaviour at different depths within the skin in this work a sensor with multiple planar electrodes is employed. The wider the distance from the driven to ground electrode, the deeper the penetration of the electric field into the tissue material.

2. Objective

The aim of this work consists of the development of a reliable, computationally efficient numerical model for the dielectric behaviour of the skin in the MHz region.

The main question hereby is, which degree of complexity is required in order to reconstruct and to be able to interpret measured dielectric data of the skin. Multiscale models with different degrees of complexity of the tissue structure are set up, based on the shape of the cells at the considered scale, the volume fraction and material composition. Finally, all models were validated by comparing them with *in vivo* measurements with and without SC.

3. Numerical modelling

3.1. Brief review on skin morphology and composition

It was found in [24] that the cell shape has a significant influence on the effective dielectric properties at frequencies <10 MHz. In order to be able to decide which features are necessary to be included in an appropriate skin model, detailed knowledge of the skin morphology is required. Therefore, a brief literature review on skin anatomy sketched in figure 1 is given in the following.

The SC contains flat hexagonally shaped corneocytes embedded in a lipid matrix forming a so-called ‘bricks-and-mortar’ structure [25–27]. The diameter of a corneocyte is 40 μm , the height 0.8 μm [28]. The intercellular distance is approximately 0.1 μm which provides a cellular volume fraction of $\varphi_{\text{corneocyte}} = 0.85$. The cytoplasm contains ceramides, free fatty acids, cholesterol, proteins (keratin) and water. In contrast to most other cells the corneocyte does not contain a nucleus. The extracellular matrix, the ‘mortar’ mainly consists of lipids and proteins and very little bound water (less than a monolayer). The total water volume fraction in the SC is 0.15–0.25, while 90% of the water is contained within the corneocyte [29, 30]. By definition the SC belongs to the epidermis, but due to the high lipid and protein and low water content it differs significantly from the lower-lying epidermal layers and is here therefore considered separately. The SC thickness depends on the body site but exhibits only little interindividual variations among healthy subjects. On the dorsal site of the upper arm the SC is approximately 20 μm thick [25–27] and [31].

The living epidermis (E) mainly consists of keratinocytes. The cuboidal to columnar epidermal cells are gap-connected and occupy a volume fraction of 0.83 [32]. The overall water volume fraction in the dermis of 0.7 is equally distributed among intra- and extracellular space [33]. The epidermis is approximately 0.1–0.2 mm [34] thick.

The transition zone between epidermis and dermis (D), the so-called dermo-epidermal junction is not planar but forms papillae with a depth of 50 μm .

The papillary dermis (PD) occupies the upper 10% of the dermis and consists of a dense collagen network [35] and blood ($\varphi_{\text{blood}} = 0.04$ [36]). The major part of the dermis, the reticular dermis (RD) consists of irregular connective tissue, lymphatic vessels, nerves, blood vessels, stromal cells such as fibroblasts and other cellular components, e.g. macrophages or plasma cells. The capillaries in the approximately 200 μm long dermal papillae are oriented perpendicular to the skin surface, while the upper vessel plexus (UVP) is a dense vascular network

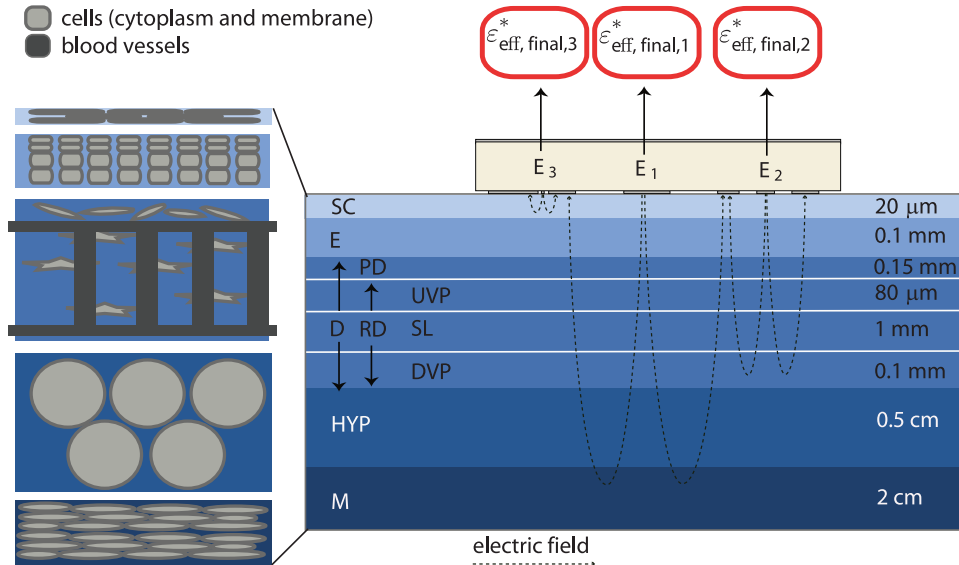


Figure 1. 2D cross-section sketch of the layered skin model consisting of stratum corneum (SC), epidermis (E), dermis (D), hypodermis (HYP) and muscle (M). In the basic model denoted as MGW (see section 3.6) the epidermis and dermis are concatenated to one single layer denoted as (E/D). In the most refined model the dermis is subdivided into papillary dermis (PD) and reticular dermis (RD), whereas the latter contains the upper vessel plexus (UVP), the supply layer (SL) and the deeper vessel plexus (DVP). A sketch of the microstructure of the skin layers is given on the left.

parallel to the skin surface ($d_{UVP} = 80 \mu\text{m}$, $\varphi_{\text{blood,UVP}} = 0.3$). The sparsely distributed blood vessels of the supply layer (SL) ($d_{SL} = 1.3 \text{ mm}$, $\varphi_{\text{blood,SL}} = 0.04$) are also perpendicular to the skin surface. The lowest layer is again a dense vascular network parallel to the skin surface, the deeper vessel plexus (DVP) ($d_{DVP} = 100 \mu\text{m}$, $\varphi_{\text{blood,DVP}} = 0.1$) [36]. The cellular volume fraction in the dermis is much smaller than in epidermis [37]. The stellar-shaped fibroblasts form a continuous network making a determination of the proper cell limits rather difficult. According to [38] the ‘body’ of the cell has an approximate diameter of $5\text{--}10 \mu\text{m}$, the extensions called stellae (4–6 per cell) are approximately $70 \mu\text{m}$ long. The collagen fibres are aligned parallel to the skin surface. Collagen is a major component embedded in the dermal matrix ($\varphi_{\text{collagen,dry}} = 0.17$ [39]). A thick collagen bundle can reach $2\text{--}15 \mu\text{m}$ in diameter. In addition to collagen and elastin the extracellular space is mainly composed of glycosaminoglycans, gelatin and sugars embedded in water.

The hypodermis (HYP) mainly consists of white fat cells, the adipocytes building the subcutaneous fat. White adipocytes are spherically shaped with a mean cell diameter of $82.6 \mu\text{m}$ [40]. The intracellular fat forms a spherical droplet pushing the cytoplasm including nucleus towards the cell membrane. The volume fraction of the lipid droplet within the cytoplasm is $\varphi_{\text{fat,intracellular}} = 0.9$ [41] the aqueous phase volume fraction is therefore only 0.1. The HYP thickness is subject to large intra- and interindividual variations.

Finally, muscular tissue (M) consisting of tightly packed narrow cigar-shaped cells is situated beneath the HYP. Muscle cells are oriented with their long axis parallel to the long axis of the humerus (upper arm bone).

Other features such as hair follicles, sweat ducts and sebaceous glands cross the entire skin down to the HYP and are mentioned for completeness.

3.2. Method description

Due to the high computational cost it is currently not realistic to simultaneously model the fringing field sensor system applied to the skin down to the single cell level. The scale of a cell membrane is in the range of nanometres while the electrode distance is up to a few millimetres. Therefore, alternatives for transferring structural information from micro- to macroscale have to be found.

An attempt to numerically model the effective dielectric parameters of the skin in the MHz frequency range is e.g. presented in [42]. The skin is subdivided into three layers (SC, E/D and HYP) according to the different water contents of these tissue types. Then, Cole–Cole models from the literature are assigned to each layer and in a FEM simulation the layered system is probed by a fringing field probe geometry (coaxial probe and the sensor introduced in section 3.5). However, as already mentioned, in this work Cole–Cole models are not considered for the dielectric parameters of tissue types because of the difficult assignment of spectral features to the microstructure.

The setup of a general dielectric tissue model for quasi-static electric fields is presented in the following and applied to the skin. The principal idea is to consider tissue as a quasi-periodic structure exposed to a homogeneous external electric field [24] and to perform a one- or multi-step homogenization procedure in order to grasp the different scales of the tissue’s microstructure. By defining a cubic unit cell of the structure (containing one biological cell embedded in extracellular medium in the simplest case of simple cubic packing) the complex effective dielectric tensor $\bar{\epsilon}_{\text{eff}}^*$

$$\bar{\epsilon}_{\text{eff}}^* = \begin{pmatrix} \epsilon_{xx,\text{eff}} & 0 & 0 \\ 0 & \epsilon_{yy,\text{eff}} & 0 \\ 0 & 0 & \epsilon_{zz,\text{eff}} \end{pmatrix} \quad (1)$$

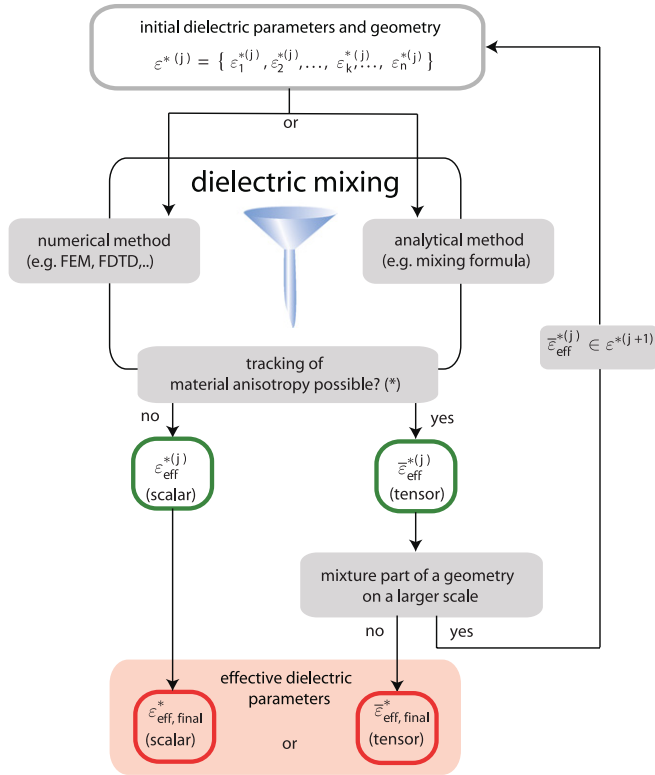


Figure 2. Schematic of the dielectric homogenization procedure for a material with (quasi-) periodic structures on one or more scales. Depicted is the step for one hierarchy or scale step, j . (*) The tracking of the anisotropy of the material is only possible if the geometry consists of a cubic unit cell with walls parallel to the xy -, yz - and xz -planes and the electric field is applied to the z -, x - and y -direction, respectively in order to obtain the dielectric tensor of the material.

can be calculated. If the tissue contains quasi-periodic structures on a smaller (subcellular) or larger (mesoscopic) scale the procedure can be iteratively repeated in a sort of recursion scheme by starting at the smallest scale, calculating the effective dielectric parameters of the unit cell, building up a structure in a new unit cell on the next-higher scale with assigned material parameters from the previous scale, again calculating the effective parameters of this new unit cell, and so on. For a better understanding the general procedure is displayed in figure 2. The first step in the application of the homogenization scheme to human skin consists of a subdivision into macroscopic layers. Then each layer is investigated with respect to the underlying quasi-periodic structures. Some skin layers only contain quasi-periodicity on the cellular scale (single biological cell composed of water and fatty, dry biological material), other skin layers suggest the use of a multi-step homogenization, as e.g. the dermis. For each layer $\bar{\epsilon}_{\text{eff}}^*$ and its dispersive features are then analytically or numerically calculated and finally inserted into the numerical macroscopic model. The overall procedure for the model with the highest complexity is later depicted in figure 2. Except for muscle tissue the skin is supposed to be isotropic in the x - y -plane (if the z -axis of the coordinate system is perpendicular to the layer boundaries) and the effective dielectric tensor

reduces to

$$\bar{\epsilon}_{\text{eff}}^* = \begin{pmatrix} \epsilon_{xx,\text{eff}} & 0 \\ 0 & \epsilon_{zz,\text{eff}} \end{pmatrix} \quad (2)$$

in the 2D model. The final skin models are experimentally validated as described in section 4. As the SC has a large influence on the effective dielectric properties its removal is used as an additional validation criterium.

3.3. Quasi-static analysis

As the smallest wavelength of the electromagnetic field and the skin depth are much larger than the overall sensor geometry, a quasi-static approximation of the problem can be applied. In the absence of external current sources an electro-quasi-static approximation of the Maxwell equations neglecting the induction voltage $\partial/\partial t \vec{B} = \vec{0}$ results in

$$\nabla \times \vec{E} = \vec{0}, \quad (3)$$

$$\nabla \times \vec{H} = \frac{\partial}{\partial t} \vec{D} \quad (4)$$

as well as in the necessary condition for the electric potential φ

$$\vec{E} = -\nabla\varphi \quad (5)$$

where \vec{E} is the electric, \vec{H} , the magnetic field strength and $\vec{D} = \epsilon^* \vec{E}$ the electric flux density. The complex permittivity is defined as $\epsilon^* = \epsilon_0 \epsilon_r = \epsilon_0 (\epsilon' - j\epsilon'')$. Because of the quasi-static approximation, only the electric potential φ has to be evaluated according to the following equation:

$$\nabla \cdot \left(\epsilon^* \nabla \frac{\partial}{\partial t} \varphi \right) = 0. \quad (6)$$

Our analysis consists of establishing the numerical model encompassing the probe and multilayer system under test, the calculation of the system's admittance Y and finally, the extraction of the effective dielectric properties.

For the numerical evaluation the finite-element method (FEM) based commercial simulation software COMSOL Multiphysics® version 3.5a is used. Although it is possible to model certain probe geometries such as coaxial probes or interdigitated sensors on top of multilayer systems semi-analytically [43–45] a numerical analysis has been chosen because the multi-electrode sensor does not fall into one of these categories. In the following, the terms permittivity and conductivity are used as $\epsilon = \epsilon'$ and $\sigma = \sigma_{\text{DC}} + \omega \epsilon_0 \epsilon''$.

3.4. Extraction of dielectric parameters

The solution of the numerical simulation provides the input admittance of the system consisting of a probe and material under test (i.e. the three-layer system). The effective dielectric parameters are extracted using the standard determination procedure of determination of the measurement cell's cell constants [46]. In the equivalent circuit the admittances $Y = G + j\omega C$ of probe and material under test are in parallel. The real parts of the effective permittivity and conductivity ϵ_{eff} and σ_{eff} for a material under test are then given by

$$\epsilon_{\text{eff}} = \frac{C_{\text{material}} - k_p}{k_m}, \quad (7)$$

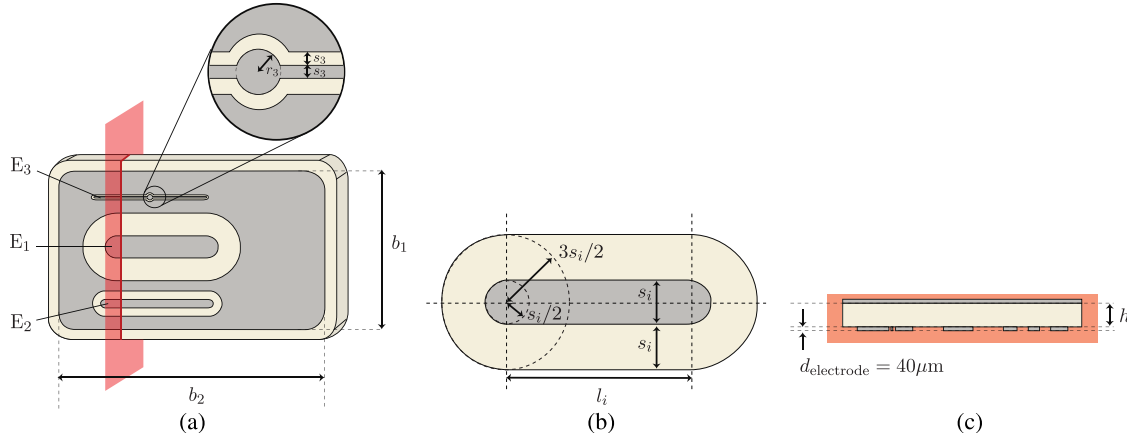


Figure 3. (a) Multi-electrode sensor with a ground plane of size $b_1 = 28$ mm and $b_2 = 47$ mm. (b) Electrode and gap dimensions of E_i . The electrode widths are equal to the gap widths: $s_1 = 4$ mm (E_1), $s_2 = 1.5$ mm (E_2) and $s_3 = 0.3$ mm (E_3). The electrode lengths are $l_1 = 16$ mm, $l_2 = 18.5$ mm and $l_3 = 19.8$ mm. The circular patches at the electrode ends have radii equal to $s_i/2$. The radius of the circular patch in the centre of E_3 is $r_3 = 0.5$ mm. The substrate thickness h_s is 1.6 mm, the material Rogers RO4350b with $\epsilon_r = 3.48$ and $\sigma = 0$. (c) Sensor cross-section. The electrode thickness is $d_{\text{electrode}} = 40 \mu\text{m}$.

$$\sigma_{\text{eff}} = \frac{G_{\text{material}} \epsilon_0}{k_m}. \quad (8)$$

The cell constants of the measurement cell, k_m and k_p are required in order to remove the probe's contribution to the admittance. The characteristics of the geometry is though still contained in the electric field pattern. The cell constants can be calculated when the admittances of two materials with known dielectric parameters are determined. In this measurement procedure, one material is air, the second material usually water or an aqueous electrolyte solution, as NaCl(aq) or KCl(aq)

$$Y = Y_{\text{probe}} + Y_{\text{material}}. \quad (9)$$

The cell constants are calculated according to

$$k_m = \frac{C_{\text{NaCl(aq)}} - C_{\text{air}}}{\epsilon'_{\text{NaCl(aq)}} - 1}, \quad (10)$$

$$k_p = C_{\text{air}} - k_m. \quad (11)$$

Equations (7) and (8) are used in the following in order to determine the effective dielectric parameters of the skin model.

3.5. Sensor setup

The sensor contains three strip-like electrodes E_i with different gap widths s_i . The electrode widths for each electrode are the same as the corresponding gap widths: $s_1 = 4$ mm (E_1), $s_2 = 1.5$ mm (E_2) and $s_3 = 0.3$ mm (E_3), as shown in figure 3(b). The lengths of the electrodes are $l_1 = 16$ mm, $l_2 = 18.5$ mm and $l_3 = 19.8$ mm. The circular patches at the electrode ends have radii equal to $s_i/2$. The radius of the circular patch in the centre of E_3 is $r_3 = 0.5$ mm. The total area of the sensor is $A_{\text{sensor}} = 1316 \text{ mm}^2$. A Rogers RO4350b substrate with thickness $h_s = 1.6$ mm and $\epsilon_r = 3.48$ ($\sigma = 0 \text{ S m}^{-1}$) is separating the electrodes from the ground plane on the backside of the sensor. The electrodes are fed by coaxial connectors on the backside of the sensor, where the inner conductors extend to vias contacting the middle of each

electrode. Similarly to the coaxial probe, the multi-electrode sensor is a capacitive probe with negligible inductance for frequencies up to several 100 MHz. Above a certain frequency the sensor starts to resonate and act as an antenna. However, according to measurements (not shown here) these resonances occur above 100 MHz for all three electrodes.

The overall macroscopic model including sensor and skin model exhibits small details in a large overall geometry. A 3D FEM simulation of a typical dielectric spectroscopy system including the multi-electrode sensor and skin model consists of approximately 1.6 million mesh cells, which uses 65 GB of RAM and takes a computation time of around 2 h per frequency point. This is why appropriate 2D approximations of such structures are desirable. The relative deviation of a 2D approximation (using the sensor cross-section in figure 3(b)) with respect to a 3D reference simulation is shown in figure 8.

In the macroscopic model the skin is assumed to consist of layers parallel to the skin surface (x - y -plane). A simple model has been introduced in [42]. It consists of three layers (SC, epidermis/dermis and hypodermis) and the dielectric parameters are given by Cole–Cole fits to measured data in [17, 18]. This model is employed in section 5.1 in order to investigate to what extent the full 3D model can be replaced by a 2D approximation.

3.6. Skin models and scaling hierarchies

As already mentioned, the first macroscopic subdivision of skin happens according to the water content of the layers. It was found in [42] that for the model of intact skin with SC a model down to the HYP is sufficient, i.e. the electric field does not penetrate beyond this layer. However, after removal of the rather insulating SC the penetration depth extends down to muscle tissue assuming a HYP thickness of 5 mm extracted from the MR image. Therefore, muscle is included in the model as well.

The contribution of hair follicles, sweat glands and sebaceous glands mentioned in section 3.1 is not supposed

Table 1. Overview of the skin models.

Model	Mixing formula	Number of phases per skin layer	Anisotropy
MGW	MG	2	No
MGI	MG	3 or more	No
LOI	LO	3 or more	No
MGA	MG	3 or more	Yes
HBA	HB	3 or more	Yes
NUM	Numerical (SC, E, HYP) and HB (D and M)	3 or more	Yes

to be negligible (especially the sweat ducts occasionally filled with sweat) but estimated to be more or less equal for all skin layers, leading to a certain but more or less equal offset in the dielectric properties. Furthermore, hair follicles and glands are not filled with cells and therefore not part of the presented model, because mainly the cells are observed to provide a significant contribution to the material dispersion in the lower MHz range [24].

After defining the macroscopic model the dielectric properties of each of the sublayers have to be defined. The complexity of the different models follows the subsequential inclusion of features that are likely to affect the dielectric spectrum. In the MHz region the β -dispersion, the short-circuiting of the cell membranes [47] is the dominant feature and has therefore to be reproduced by a valid model. Other dispersion mechanisms such as electrode polarization and α -dispersion below 1 MHz and the relaxation of free water (γ -dispersion) in the low GHz region occur outside of the considered frequency range. Therefore, those mechanisms are said not to affect the spectrum in the MHz range and are not included in the model. The weak δ -dispersion above 100 MHz caused by the relaxation of bound water and proteins might extend into the upper part of the frequency region of interest between 1 and 100 MHz, but is neglected here because of its weakness compared with the β -dispersion. From the structural point of view on the subcellular scale the simplification with the largest impact consists of not including organelles and cell nucleus in the models.

In the following, the models for the effective properties of each layer are introduced. The model order follows a hierarchy given by the increasing degree of complexity in terms of number of layers as well as number of components and stages for the homogenization of the dielectric parameters. An overview of all models is given in table 1.

Potential sources of error or variation are electrode surface roughness, the influence of a potentially occurring air or sweat layer or pressure variations and structural features crossing the entire skin (sweat ducts, hair follicles). However, the inclusion of trans-layer features is out of scope of this work.

3.6.1. MGW model—layers of aqueous, biphasic Maxwell–Garnett (MG) mixtures. A first model refinement consists of modelling the skin layers as two-phase mixtures. Biological tissue in general mainly consists of an aqueous phase (extracellular liquid, cytoplasm) and a lipid phase (cell

membrane, intra- and extracellular lipids) being distinct from a dielectric point of view. The aqueous phase basically consists of water and electrolytes with the approximate dielectric parameters $\epsilon_1^{(1)} = 78$ and $\sigma_{DC,1}^{(1)} = 1.2 \text{ S m}^{-1}$. On the other hand, the lipid phase approximated by oleic acid has a low permittivity $\epsilon_2^{(1)} = 2.5$ and is practically non-conducting $\sigma_{DC,2}^{(1)} = 0 \text{ S m}^{-1}$ [48]. Since the water contents of the skin layers differ significantly ($\varphi_{\text{water,SC}} = 0.2$ [30], $\varphi_{\text{water,E}} = 0.7$, $\varphi_{\text{water,D}} = 0.7$, $\varphi_{\text{water,HYP}} = 0.25$ [36] and $\varphi_{\text{water,M}} = 0.8$), the volume fractions of the aqueous and lipid phase, respectively, a simple two-phase model is set up in order to characterize each layer. The effective dielectric parameters $\epsilon_{\text{eff}}^{(1)}$ and $\sigma_{\text{eff}}^{(1)}$ of the so-defined binary mixtures are calculated with the MG mixture formula [49] in equation (12).

$$\frac{\epsilon_{\text{eff}}^{*(j)} - \epsilon_1^{*(j)}}{2\epsilon_{\text{eff}}^{*(j)} - \epsilon_1^{*(j)}} = \varphi_2^{(j)} \frac{\epsilon_2^{*(j)} - \epsilon_1^{*(j)}}{2\epsilon_2^{*(j)} - \epsilon_1^{*(j)}}. \quad (12)$$

Here, $j = 1$ and material 2 is embedded in material 1. Equation (12) provides the analytical first-order solution for the effective permittivity of a spherical inclusion for volume fractions up to 0.1, but since geometry is not considered in this model it actually has no significance. The dielectric parameters for this model are all scalar.

3.6.2. MGI, LOI, MGA and HBA models—layers of multiphasic MG, Looyenga and Hanai–Bruggeman (HB) mixtures. For the following models, the initial subdivision of skin into three layers is refined. The layer thicknesses are the following: $d_{\text{SC}} = 20 \mu\text{m}$, $d_{\text{E}} = 100 \mu\text{m}$, $d_{\text{D,PD}} = 150 \mu\text{m}$, $d_{\text{D,UVP}} = 80 \mu\text{m}$, $d_{\text{SL}} = 1 \text{ mm}$, $d_{\text{DVP}} = 100 \mu\text{m}$, $d_{\text{HYP}} = 5 \text{ mm}$. Finally, muscle tissue terminates the model ($d_{\text{M}} = 2 \text{ cm}$, ∞). The system consisting of sensor and layer structure is depicted in figure 1.

$$\int_0^{\varphi_2} \frac{d\varphi_2'}{1 - \varphi_2'} = \int_{\epsilon_1^*}^{\epsilon_{\text{eff}}^*} \frac{3}{\epsilon_{\text{eff}}^*} \left[\sum_{k=x,y,z} \frac{\epsilon_{\text{eff}}^* - \epsilon_2^*}{\epsilon_{\text{eff}}^* + (\epsilon_2^* - \epsilon_{\text{eff}}^*)L_k} \right]^{-1} d\epsilon_{\text{eff}}^*, \quad (13)$$

$$\epsilon_{\text{eff},2(n)}^* = \epsilon_n^* \times \left(1 + \frac{\frac{a_{x,n+1}a_{y,n+1}a_{z,n+1}}{a_{x,n}a_{y,n}a_{z,n}} (\epsilon_{n+1}^* - \epsilon_n^*)}{\epsilon_n^* + (\epsilon_{n+1}^* - \epsilon_n^*)L_{n+1} - \frac{a_{x,n+1}a_{y,n+1}a_{z,n+1}}{a_{x,n}a_{y,n}a_{z,n}} (\epsilon_{n+1}^* - \epsilon_n^*)L_n} \right). \quad (14)$$

A first attempt to truly incorporate microstructural information into a skin layer model is undertaken by approximating single tissue cells by shelled ellipsoids. This has already been performed in order to calculate dielectric parameters of e.g. suspensions of *E. coli* cells [50], red blood cells [51] or rat liver tissue [52]. Since the MG formula can be generalized for multi-shelled confocal ellipsoids [53] it is employed here in order to calculate the effective dielectric parameters of the skin layers modelled as a suspension of randomly oriented (model MGI) and aligned (MGA) single-shelled confocal ellipsoids. The cell dimensions, volume fractions and material compositions were estimated based

Table 2. Material and geometrical parameters for the models MGI, MGA, LOI and HBA. Each layer within a model provides a dielectric tensor $\bar{\epsilon}^{*,(j)}$ which is inserted into the macroscopic model. Some phases at scale level j are already mixtures with $\bar{\epsilon}^{*,(j-1)}$ at a lower scale.

Sub-phase		Geometry				Materials		
Skin layer	Shape of inclusion	$\varphi_{\text{inclusion}}$	$(d_x \ d_y \ d_z) (\mu\text{m})$	$(d_{\text{shells}}) (\text{nm})$	Phase	Dielectric parameters		
						$\epsilon_i^{(j)}$	$\sigma_{\text{DC},i}^{(j)} (\text{S m}^{-1})$	
SC extracellular	Inclusion Sphere	0.95			Extracellular medium	80	0.53	
					Dry biological material	2.5	0	
SC cytoplasm	Inclusion Sphere	0.8			Extracellular medium	80	0.53	
					Dry biological material	2.5	0	
SC	Inclusion Shelled ellipsoid	0.91	(20 20 0.8)	7	SC extracellular	9.04	10^{-6}	
					Cell membrane	9.04	10^{-6}	
E	Inclusion Shelled ellipsoid	0.83	(5.97 5.97 11.95)	7	SC cytoplasm	80	0.53	
					Extracellular medium	80	0.53	
	Collagen	Inclusion Cylinder	0.17	$(\infty \ 100 \ 100)$	7	Cell membrane	9.04	10^{-6}
						Cytoplasm	50	0.12
Dermis 'matrix'	Inclusion Shelled ellipsoid	0.315	(70 70 7)	7	Extracellular medium	80	0.53	
					Collagen (xy-isotropic)	80	0.53	
D	UVP	Inclusion Cylinder (xy-isotropic)	0.3	$(\infty \ 50 \ 50)$	7	Cell membrane	9.04	10^{-6}
						Cytoplasm	50	0.12
	SL	Inclusion Cylinder	0.04	(50 50 ∞)	7	Dermis 'matrix'	[18]	[18]
DVP	Inclusion Cylinder (xy-isotropic)					0.1	$(\infty \ 50 \ 50)$	7
HYP		Inclusion Double-shelled sphere	0.8	(45 45 45)	7			
	$\varphi_{\text{fat}} = 0.771$					3.76×10^3	Dermis 'matrix'	[18]
	Inclusion Shelled ellipsoid	0.85	(0.5 2 0.5)	7	Blood ^a		[18]	[18]
					Extracellular medium	80	0.53	
M	Inclusion Shelled ellipsoid	0.85	(0.5 2 0.5)	7	Cell membrane	9.04	10^{-6}	
					Cytoplasm	50	0.12	

^a The parameters for blood are frequency dependent.

on the literature values given in section 3.1. The dielectric parameters for extracellular medium, cell membrane and cytoplasm were set according to [54]. All geometrical and material parameters are given in table 2. It is necessary to mention that the shelled ellipsoids used in the calculation were not confocal (equal foci) but concentric (constant shell thickness each surface point). But since the membrane thickness $d_m = 7 \text{ nm}$ is much smaller than the cell dimensions this approximation is considered as justified.

Compared with the relatively straightforward representations of SC and HYP the modelling of the epidermis and dermis imposes some challenges. Although the water content is similar in dermis and epidermis ($\varphi_{\text{water}} = 0.7$) a unified morphological description of the two layers is rather difficult. The structural properties even suggest subdividing at least the dermis into sublayers. The cellular volume in the dermis is so small that the influence of the cell shapes on the dielectric properties will probably be much smaller than the other

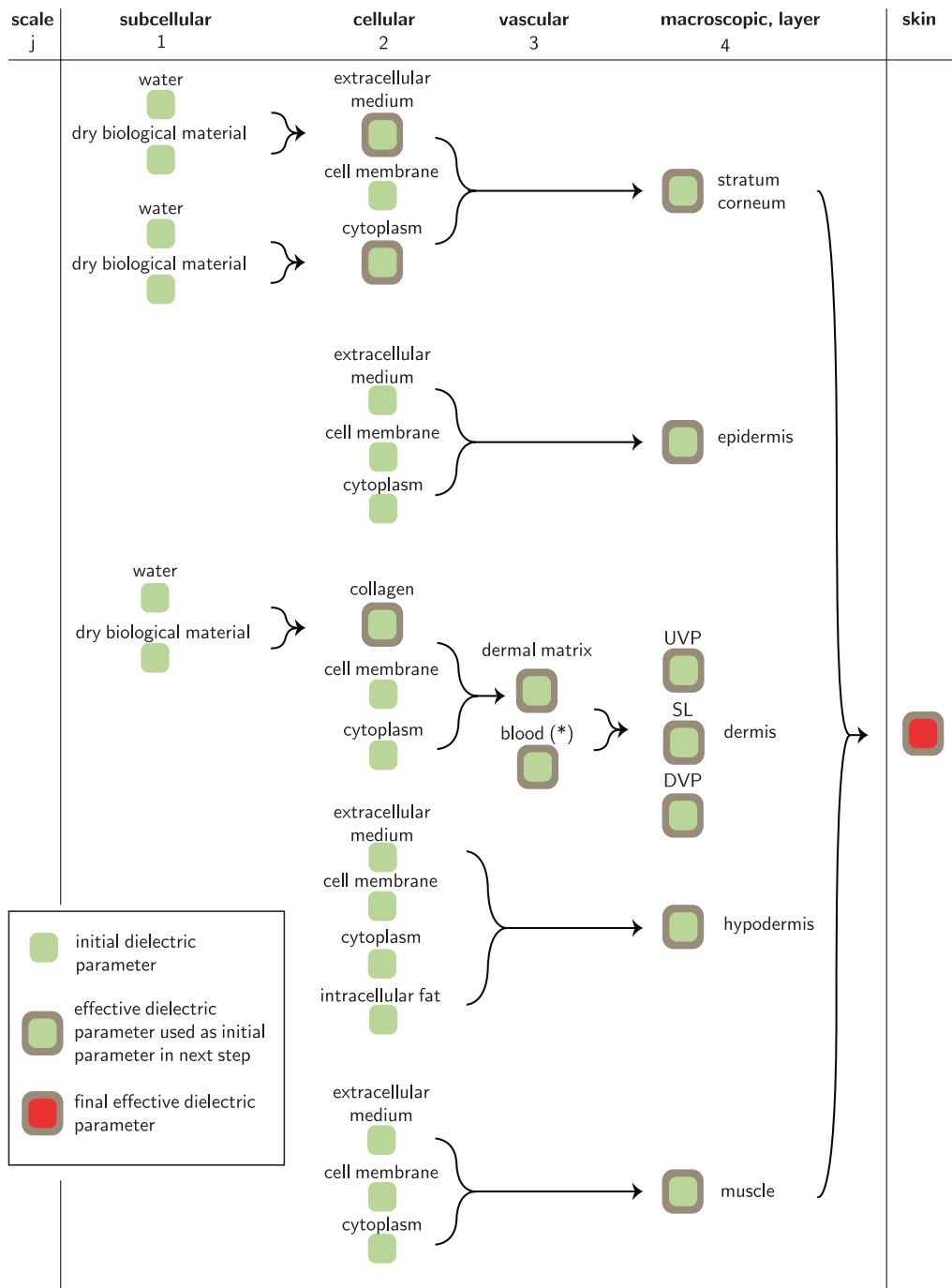


Figure 4. Complete mixing scheme for the final dielectric human skin model (NUM). (*) The effective parameters for blood were taken from [18]. Abbreviations for dermis subdivision: upper vessel plexus (UVP), supply layer (SL) and deeper vessel plexus (DVP).

features such as the collagen network or orientation of blood vessels. Therefore, the goal for the dermis model was first, to directly or indirectly include single cells and second, to capture main anisotropy directions likely to be seen in dielectric spectra. In particular, the dermis anisotropy is not described in terms of unit cells on a single cell level anymore, but at a larger scale the distribution of blood vessels embedded in a collagen network replaces this measure. Consequently, the E/D is partitioned into the joint layer consisting of epidermis and capillary layer of the PD, the UVP the supply layer (SUP) and finally the DVP. The dimensions (scaling of the

dermis thickness obtained by MRI) and parameters for blood volume fractions were set according to [36]. The PD was entirely approximated by densely simple cubic packed columnar keratinocytes ($\varphi_{\text{keratinocyte}} = 0.83, d_x = d_y < d_z$) given in figure 5(e). The deeper lying layers were analytically modelled using the HB formula given by equation (13) for aligned cylinders in an anisotropic collagen matrix. The cylinder material consisted of blood with Cole–Cole parameters obtained from [18], the radius according to [55] for capillaries. The Cole–Cole model from [18] was utilized here for simplicity reasons. It would be also possible to approximate blood cells

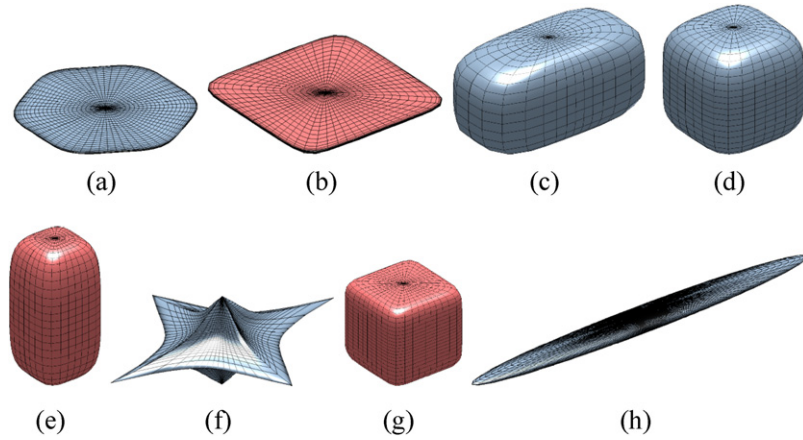


Figure 5. Estimated shapes of cells occurring in the skin parameterized with the Superformula. Only the red-coloured cell shapes ((b), (e) and (g)) were used in the NUM model. The more realistic corneocyte hexagonal shape in (a) was replaced by the D_{4h} -shape in (b) in order to model a realistic volume fraction and to be able to establish a (bcc) unit cell. The same holds for the adipocyte in (g). The corresponding shape parameters are given in table 3.

(erythrocytes, lymphocytes, etc) by ellipsoids and calculate the dielectric properties for the solid blood constituents in blood plasma. However, this was skipped here for simplicity reasons. The volume fractions of the cylinders approximating blood vessels and their orientation (perpendicular or parallel to the skin surface) were set as introduced in the previous subsection. The parameters for the collagen matrix itself were again calculated with the MG formula. The mixture consisted of collagen cylinders parallel to the skin surface, embedded in extracellular medium. The volume fraction and collagen fibre radius for collagen were taken from [56].

In the case of the MGI model the particle orientations are averaged out and the effective material is isotropic. The same holds for the LOI model: the effective dielectric properties of the inclusion (material with index $i = 2$) are calculated using the MG formula, but the final step is calculated with the Looyenga formula (LO) in equation (15):

$$\varepsilon_{\text{eff}}^{*,(j)} = \left(\varphi_2 \sqrt[3]{\varepsilon_2^{*,(j)}} + (1 - \varphi_2) \sqrt[3]{\varepsilon_1^{*,(j)}} \right)^3 \quad (15)$$

also leading to an averaging of particle orientation. Since the LO formula averages out the anisotropy and since the mixing formula is symmetric, a major part of the geometrical information is lost. On the other hand, for the MGA model $\bar{\varepsilon}_{\text{eff}}^{*,(1)}$ does not reduce to a scalar anymore and anisotropy can be accounted for. As mentioned, the MG formula is only valid for inclusion volume fractions $\varphi_{\text{inclusion}} < 0.1$ since interparticle interactions are neglected [49]. In order to overcome this restriction the HB formula given in equation (13) for a two-phase mixture (host: material with $i = 1$, inclusion: material with $i = 2$) was suggested and also extended for multi-shelled ellipsoidal particles with the homogenization step j , component number i , number of particle shell n , coordinate axis k and depolarization factor L_k . The HB formula in [57] said to be valid for volume fractions up to $\varphi_{\text{inclusion}} < 0.8$ [57]. In analogy to the MGA model, the HB solution for aligned multi-shelled ellipsoidal particles provides $\bar{\varepsilon}_{\text{eff}}^*$.

The morphological and material parameters for the MGI, MGA, LOI and HBA models are summarized in table 2.

3.6.3. NUM model—layers of partly numerically calculated multiphasic mixtures. Both, the MG as well as the HB formula impose a volume fraction limit due to interparticle interaction as well as due to the quasi-periodic structure and resulting simple cubic packing. The aim of the NUM model was to include features and aspects that are not part of the previous models but expected to affect the dielectric spectra up to the macroscale. In order to keep the computational effort reasonable, the focus in the NUM model was put once again on the following features:

- Cellular volume fraction φ
- Approximate composition of extracellular medium and cytoplasm
- Intercellular interactions (cell shape, ordering)

Since the shape of biological cells usually differs from ellipsoidal and the volume fraction in tissue often exceeds even the densest possible packing of ellipsoids ($\varphi_{\text{inclusion}} = 0.7707$ [58]) a motivation for the refinement of the MGA/HBA models arises. In terms of a more flexible geometry the effective dielectric parameters of particles can be calculated analytically using the spectral density function approach [59, 60]. But as the expressions become very complicated with increasing shape complexity numerical simulations were used in the NUM model. The cell shapes were generated with a very flexible parametrization method, the so-called Superformula introduced in [61]. With this method it is possible to model a wide variety of realistic biological shapes. Following our approach in [24] the cell is placed in a parallel plate capacitor filled with extracellular medium in order to generate the corresponding electric field background for the determination of the effective dielectric properties. Its dimensions are determined by the volume fraction of the cell and the maximal distances of the cell shape in the x -, y - and z -direction. In order to obtain the diagonal dielectric tensor $\bar{\varepsilon}_{\text{eff}}^*$ (equation (1)) as for the MGA and HBA models the electric field is first applied in x -, then in y - and finally in the z -direction with Neumann boundary conditions on boundaries perpendicular to the electrodes in each corresponding case.

Table 3. Superformula parameters for selected skin cells.

Cell type	Skin layer	Supershape parameters							Figure 5
		a	b	m	n_1	n_2	n_3	d	
Corneocyte ^a	SC	1	1	6	4	4	2	60	(a)
Corneocyte ^a D_{4h}	SC	1	1	4	8	8	8	60	(b)
Keratinocyte 1	E	1	0.5	4	4	4	4	30	(c)
Keratinocyte 2	E	1	1	4	4	4	4	30	(d)
Keratinocyte 3	E	0.5	0.5	4	4	4	4	30	(e)
Fibroblast	D	1	1	4	0.5	1	0.75	60	(f)
Adipocyte	HYP	1	1	4	4	4	4	40	(g)
Muscle cell	M	3	0.3	4	2	2	2	200	(h)

^a The corneocyte models are additionally scaled by a factor of 0.02 in the z -direction. The corneocyte D_{4h} , the keratinocyte 3 and adipocyte models were employed in the numerical (NUM) model.

This geometric setup implies as already mentioned in conjunction with equation (1) a periodic structure in the plane perpendicular to the applied electric field due to the mirror images.

The application of supershapes (shapes generated by the Superformula) in dielectric modelling of cell suspensions and tissues has already successfully been performed in [24]. Diverse types of cell shapes occurring in the skin can be mimicked using the Superformula and are listed in figure 5 (for the corresponding shape parameters see table 3). The three-dimensional ordering of the corneocytes, which can be approximated by flat hexagons ordered in a hexagonally close packed (hcp) unit cell. But since the presented procedure requires a unit cell with perpendicular walls two approximations were performed. The first approximation rendering the cell shape correctly is a body centred cubic (bcc) unit cell with hexagonal corneocytes. As it is not possible to reach the required volume fraction of $\varphi_{\text{corneocyte}} = 0.91$ [62], the second approximation consists of flattened cubes instead of hexagons in a bcc unit cell, allowing one to reach the required volume fraction. The keratinocytes of the epidermis are also modelled numerically in order to reach the desired volume fraction and to better render the shape. Even though there is a smooth shape transition from corneocyte to the basal keratinocyte—which can also be reproduced with the Superformula and is sketched in figures 5(a)–(e)—the epidermis is modelled as simple cubic (sc) packed columnar cells. Albeit the Superformula can describe even complicated shapes as fibroblast-like cells given in figure 5(f) and approximate almost any cell type, the dermis structure on the cellular level is due to the large number of constituents so heterogeneous that the NUM model employs the same model parameters for the dermis sublayers as the MGI, LOI, MGA and HBA models.

The HYP is modelled applying the same idea as for the SC. However, the densest possible packing of spheres (lipid phase of the adipocyte interior) provides only a maximal volume fraction of $\varphi = 0.744$, obtained either with hcp or bcc unit cells. As the actual adipocyte volume fraction must be higher than this value again, cuboidal-shaped cells in a bcc unit cell are employed in order to conform with the large cellular volume fraction.

4. Measurements

4.1. Measurements on skin

Dielectric measurements were performed between 5 and 100 MHz using the multi-electrode sensor shown in figure 3 connected to a HP8753ES vector network analyser. The voltage between driven electrode and ground was 1 V; the other two electrodes were set to ground, repeating the procedure for all three electrodes (denoted as E_1 , E_2 and E_3 in figure 3). The setup was calibrated with air and deionized water with known static conductivity. The left upper arm was chosen as measurement site because of its accessibility, relative homogeneity of tissue parallel to the sensor surface compared with other body parts (e.g. wrist) and ability to tightly attach the sensor on the skin. The sensor was placed on the upper arm with the longer axes of the electrodes (y -direction) being parallel to the long axis of the humerus and attached with rubber bands. The location was marked in order to ensure repeatability of the sensor placement. After measuring untreated, dry skin the SC was removed by consecutive stripping with adhesive tape [63, 64]. After each stripping the admittance was measured. The procedure was terminated after 40 strippings [64] and the SC considered to be removed. All measurements were carried out at room temperature and the dielectric parameters extracted according to the procedure described in section 3.4.

Figures 3, 11 and 12 show data obtained from four measurements on one subject on the upper arm (mean values), figures 11 and 12 also include error bars (corresponding standard deviations).

4.2. Skin layer thickness determination

Skin layer thicknesses exhibit significant intra- and interindividual variations [65, 66] and should be carefully estimated. The literature values are provided in [16, 67, 68]. In this work MRI scans of the site of dielectric measurement (location marked with a pen) were recorded in order to determine skin layer thicknesses. The instrumentation consisted of a 1.5 T Philips Achieva MRI scanner in connection with a Philips microscopy coil having an inner diameter of 23 mm and the following scan protocol: T1-weighted 3D fast field echo,

TR 600; TE 14, flip angle 90° , FOV $25 \times 25 \text{ mm}^2$, matrix 256×256 , acquired resolution $0.06 \times 0.9 \text{ mm}^2$, slice thickness 1.25 mm reconstructed to 0.4 mm , bandwidth 9.8 Hz/pixel , two signal averages, 30 slices in the coronal plane.

According to [69] the epidermis, dermis, subcutaneous fat and muscle can clearly be distinguished in figure 6. The outer high-signal zone (0.2 mm) corresponds to the epidermis (E), the low-signal zone (1.3 mm) to the dermis (D). The image suggests significant compositional differences between E and D. The thick, approximately 5 mm high-signal zone is assigned to the hypodermis (HYP). Finally, the lower-lying low-signal zone under the HYP corresponds to muscle (M). 5 mm were estimated as a mean value since the border between HYP and M exhibits a curvature. This estimation is considered as acceptable since with the presented setup the sensed volume in the depth of the HYP-M border is much smaller than for the SC-E and E-D borders. Therefore, a deviation in HYP thickness will have a much smaller impact in the model compared with a potential deviation in SC, E or D thickness.

The thickness of the SC cannot be resolved with MRI. However, it does not exhibit large variations among healthy individuals for a specific body site. Therefore, the SC thickness for the upper arm, $d_{SC} = 20 \mu\text{m}$, is adapted from the literature as mentioned in section 3.1.

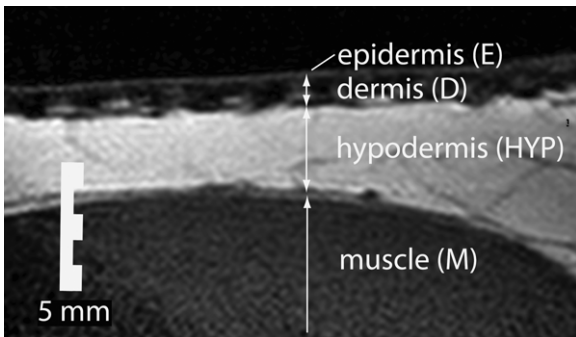


Figure 6. 1.5T MR image of the skin (dorsal upper left arm) used in determination of the skin layers on the site of the dielectric measurement. Epidermis (E), dermis (D), hypodermis (HYP) and muscle (M) can clearly be distinguished.

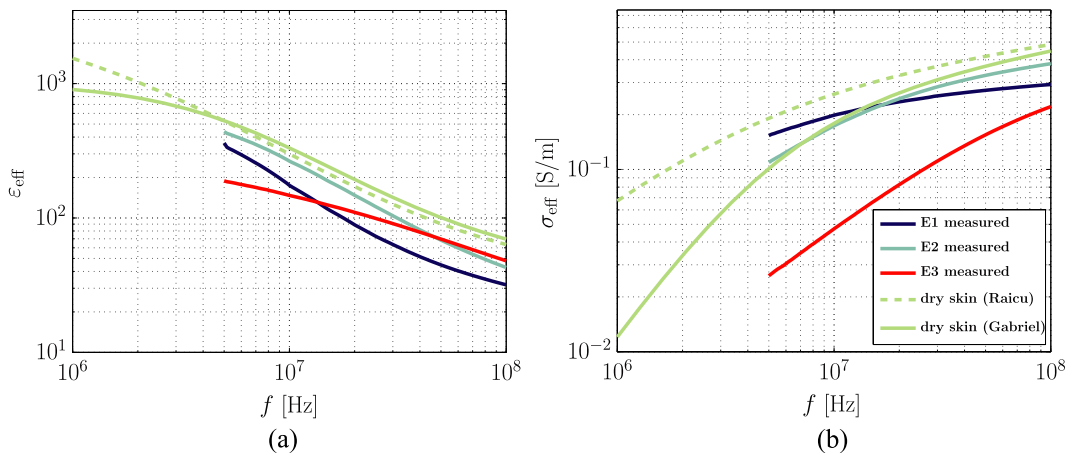


Figure 7. Comparison between effective ϵ_{eff} (a) and σ_{eff} (b) of dry skin measured with the multi-electrode sensor shown in figure 3 and parameters obtained from measurements with coaxial probes of different sizes from the literature [18, 19].

5. Results and discussion

According to the ϵ_{eff} and σ_{eff} spectra in figure 7 the measured data before stripping lies in the same range and exhibits a very similar characteristic to the literature values obtained from measurements of dry skin with open-ended coaxial probes [18, 19]. Above 200 MHz (not shown in figure 7) resonances connected to the electrical length of the electrode/sensor system occur. Therefore above 200 MHz , the quasi-static regime does not suffice anymore and a full-wave numerical model of the sensor and tissue multilayers would be required in order to correctly reproduce the measured data. In order to avoid effects due to electrode polarization, measurement inaccuracies of the vector network analyser at low frequencies and the mentioned resonances the frequency region of interest was reduced to the range from 5 to 100 MHz for measurements. However, the modelling was performed down to 1 MHz .

5.1. Comparison of 2D approximation and the 3D scenario

The full 3D system consisting of sensor and skin model is computationally expensive in terms of CPU time and RAM. This is especially challenging if many simulations, e.g. for the presented sensitivity analysis that has to be performed. Hence, it is desirable to reduce the computational effort of those simulations. One approach is to approximate the 3D geometry by a 2D representation as performed in this paragraph. The most important parameter of the multi-electrode sensor is the electrode spacing, whereas the length of the electrode exhibits a smaller influence. In the following, the electrodes are assumed to be infinitely long allowing for a 2D simulation. In this way, only the 2D cross-section of the electrode has to be modelled, resulting in a large computational speedup. A 2D simulation of the multi-electrode sensor consumes approximately 8% computer memory and 0.6% CPU time of the corresponding 3D problem. The relative deviation with respect to a 3D reference simulation is shown in figure 8. The largest relative error (with respect to the 3D model) of approximately 12% exhibits electrode E_3 .

An additional simplification of the 2D cross-section was performed by simulating each electrode of the sensor as a

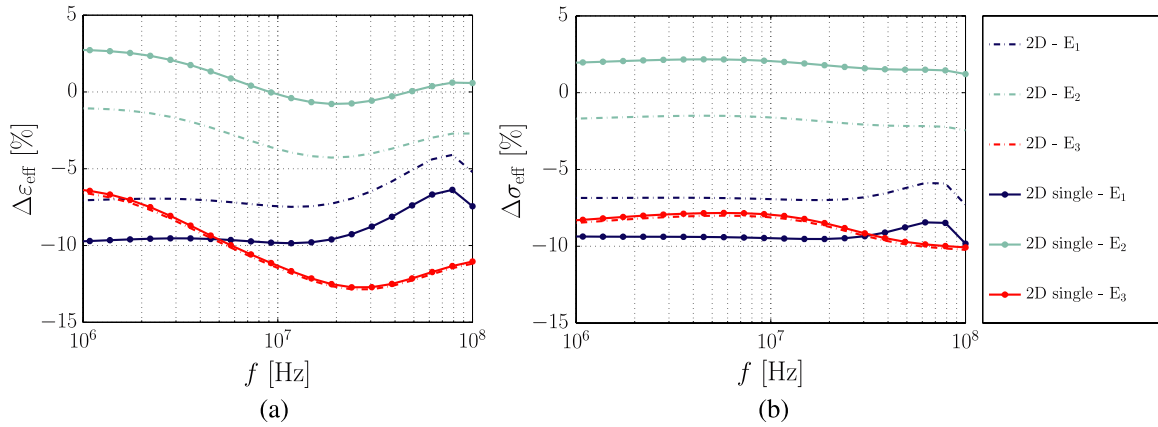


Figure 8. Relative deviations in effective permittivity $\Delta\epsilon_{\text{eff}}$ (a) and conductivity $\Delta\sigma_{\text{eff}}$ (b) of the 2D model from the 3D simulation of a simplified three-layer skin model probed by the multi-electrode sensor shown in figure 3.

2D cross-section separately. In this manner the size of the problem matrix can be further reduced, which is relevant in the case of limited computational resources. The driven electrode has the width s_i and is again separated by s_i on each side from the left and right ground electrode. The widths of the ground electrodes correspond to half the sum of the grounded electrodes from the original 2D sensor cross-section. The corresponding deviations from the full 3D model are also displayed in figure 8 and denoted as ‘ E_i —single electrode’. It can be seen that this simplification is appropriate for the smallest electrode E_3 but leads to a significantly larger error for the electrode E_1 .

In conclusion, the 2D model of the complete sensor was considered as a good approximation of the real structure yielding results which indicate the characteristics of the sensor. Therefore, this 2D model was used in the following. It has to be mentioned that, especially in the presented model with the very thin topmost layer, the electrode thickness of $40\ \mu\text{m}$ of the sensor electrodes has to be included in the model. The difference between infinitely thin electrodes and electrodes with finite thickness of $40\ \mu\text{m}$ reaches up to 20% for the smallest electrode E_3 . This has to be considered if the material under test is touching the substrate. Therefore, there is a large difference between sensing a solid, soft surface and a liquid.

5.2. Skin models

The dielectric parameters and thicknesses of SC, viable skin and HYP are in such a relation that a layered model with each layer’s water content as a characteristic parameter (model MGW) generates a relaxation in the lower MHz region due to the thin (compared with the inter-electrode distance) poorly conductive SC between electrode and viable skin. On the other hand, measurements of skin also exhibit a strong dispersion in this region due to the mentioned β -dispersion [18] caused by interfacial polarization at the cell membranes. In order to test the suitability of the models the SC was removed. Measurements show a prominent increase in both ϵ_{eff} and σ_{eff} for the E_3 and E_2 electrode and a decrease in ϵ_{eff} and increase in σ_{eff} for the E_1 electrode after removal of the SC. As expected the MGW model could not reproduce this behaviour. The contrast between viable skin and subcutaneous fat is too poor because the

E/D is about 2 orders of magnitude thicker than the SC and has larger permittivity and especially conductivity. Therefore, the observed values will not be reconstructed by the model because the contribution of the layering to the total spatial dispersion is very small. These results also indicate that the hypothesis, where the SC is strongly contributing at lower frequencies and E/D dominating at higher frequencies ($> 100\ \text{MHz}$) [63] might be inadequate. The contribution can be equal but caused by other parameters such as by the water content for whose the contrast between layers is smaller. This could e.g. be assessed by evaluating the electric energy and resistive heating in the layers. An additional argument against a significant lack of contribution of the SC is also provided in [47].

Furthermore, according to [18] the two-phase formulae are reliably applicable only at frequencies above 400 MHz, which makes sense because in the lower MHz range β -dispersion dominates and masks the influence of free water.

Modelling the ϵ and σ of each layer as shelled particles embedded in a host medium is a good initial approximation in order to reproduce trends based on morphological parameters and material composition on the cellular level, even though the initial presented MGI model is not accurate yet. With the LOI model a small improvement is achieved by averaging out the deviations from realistic cell shapes. The comparison between the models MGI/LOI and the MGA model shows that the oriented ellipsoidal particles resulting in anisotropic dielectric parameters (especially for SC) also provide a better reproduction of the measured data than isotropic mixtures of randomly oriented particles. The MGA model qualitatively reproduces the observed frequency dispersions in the measurements after removal of the SC (rise of ϵ_{eff} and σ_{eff}), at least for the E_2 and E_3 electrodes. For E_1 , the decrease in ϵ_{eff} could not be reproduced. However, it has to be noted that the penetration depths of the electric fields of E_2 and E_3 are smaller than of E_1 and therefore the accumulated uncertainty due to assumptions on layer properties as well. Several aspects such as anisotropic bound water shells [51] or the inclusion of organelles [57] can be accounted for already using an analytical or semi-analytical mixing rule. A comparison between the MGA and HBA models from figures 9 and 10 shows an even better agreement of the HBA model with the measurement data due to the account for high cellular volume fractions.

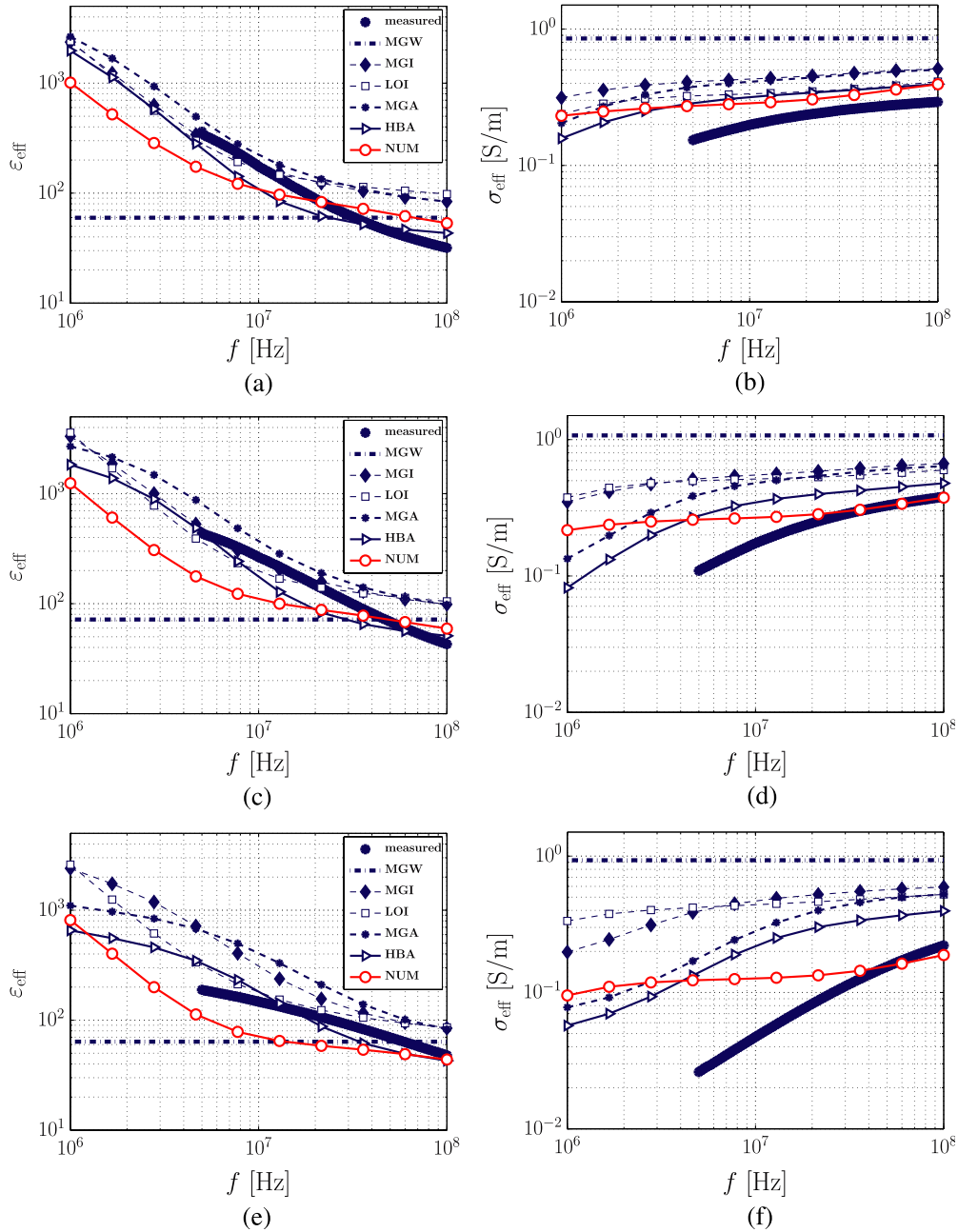


Figure 9. Effective permittivity and conductivity of intact skin probed by three different electrodes of the multi-electrode sensor from figure 3: electrode E_1 in (a) and (b), electrode E_2 in (c) and (d) and electrode E_3 in (e) and (f). Measured data (mean value for all measurements of one subject) and all models.

While inspecting the dispersion spectra in figures 9 and 10, an overall comparison of all models suggests that the NUM model is most suitable for the reproduction of the dispersion characteristics of the skin and in addition has the largest potential for improvement due to the flexibility concerning cell shape and inclusion of further details. The NUM model without SC provides a good agreement with the measured data. Figures 11 and 12 show the measured data and data obtained from the NUM models. The NUM model of intact skin suggests that the SC might be less conductive than modelled. It is very likely, that an adjustment of the conductivity of the water phase in the SC also shifts the dispersion characteristics towards the measured data. The dependence of the dielectric

parameters on the gap widths of the electrodes also indicated a similar direction of model improvement.

An additional advantage of the NUM model consists in the ability to model wet skin. In dry skin the volume fraction of extracellular water is very small. By wetting the skin this volume fraction increases, which can be easily incorporated into the model. It was shown previously in e.g. [19, 70] that the permittivity and conductivity of wet skin is significantly larger than for dry skin. This can be explained with the increase in dielectric contrast between extracellular medium and cell membrane and also between cytoplasm and membrane. If exposed to water the corneocytes themselves start to absorb water, so the intracellular water volume fraction increases as well.

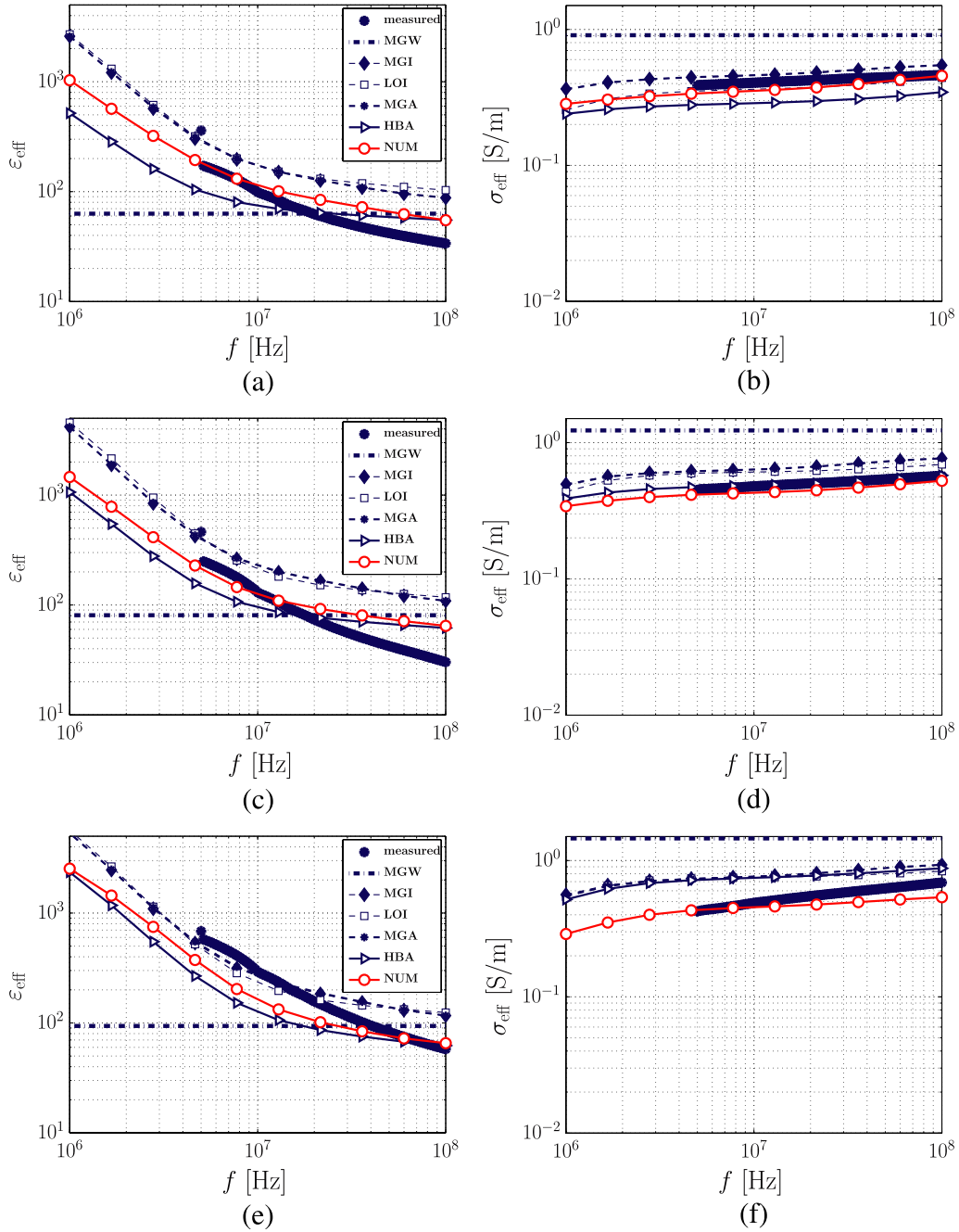


Figure 10. Effective permittivity and conductivity of skin without SC probed by three different electrodes of the multi-electrode sensor from figure 3: electrode E_1 in (a) and (b), electrode E_2 in (c) and (d) and electrode E_3 in (e) and (f). Measured data (mean value for all measurements of one subject) and all models.

6. Conclusion

The presented results suggest the need for a dielectric multiscale model of human skin in the frequency range between 1 and 100 MHz. The model with the biphasic water mixtures fails to reproduce the skin’s dielectric properties after removal of the SC. The latter model type characterized only by the water content of each layer as the relevant parameter is only applicable above 400 MHz as reported previously. Below 100 MHz at least the basic structure of tissue (cells) has to be taken into account in order to correctly reproduce the spectral signature. Shelled-particle MG- or HB-mixtures

already provide correct trends. Comparing measurement and simulation the model containing dielectric parameters of numerically calculated cell-like structures with more realistic shapes resulting in anisotropic effective dielectric properties for each skin layer provides the best results. The removal of the SC as a validation criterion for the need for at least three-phase mixtures containing approximated cells was successfully proven. The presented analysis together with the validation suggest that our multiscale model is prone to adaptation to other tissues with different cell morphologies and material composition. Model refinement is expected to happen after incorporation of mass transport on the microscale.

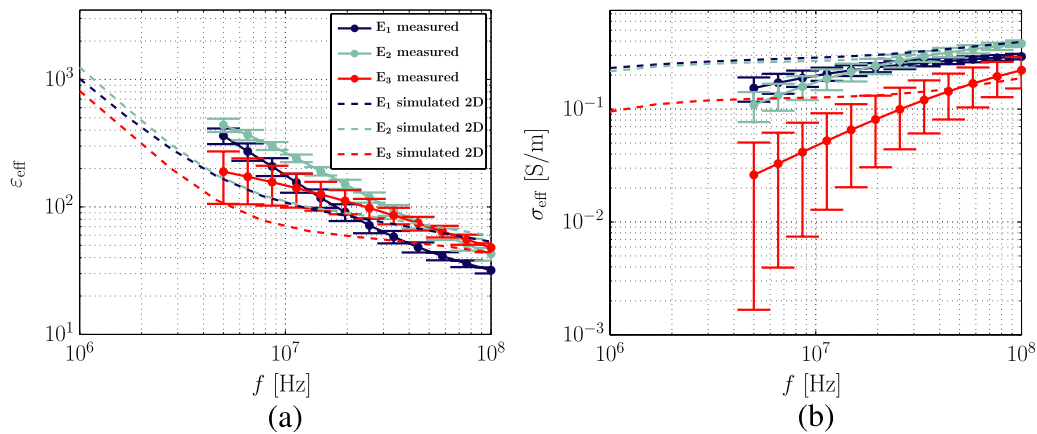


Figure 11. Effective permittivity (a) and conductivity (b) of measured (mean value for four measurements of one subject and corresponding standard deviation) and modelled (NUM model) intact skin.

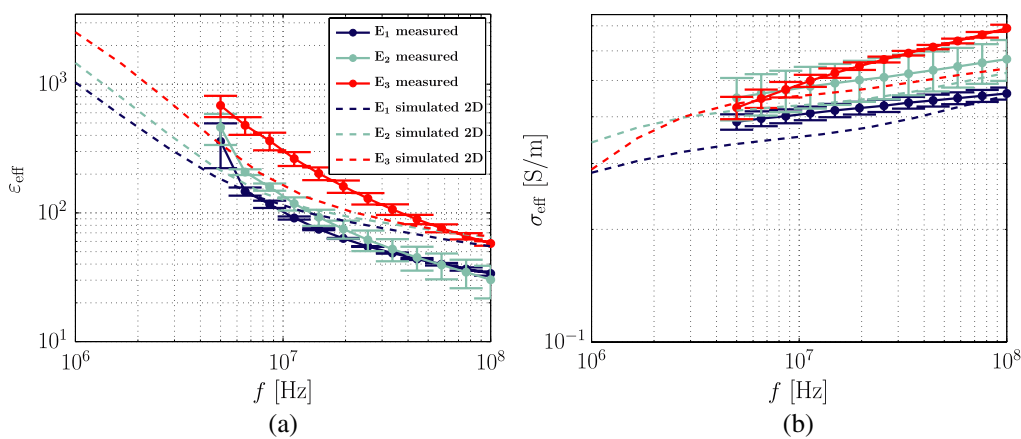


Figure 12. Effective permittivity (a) and conductivity (b) of measured (mean value for four measurements of one subject and corresponding standard deviation) and modelled (NUM model) skin without SC.

This would enable assessment of the sensitivity of dielectric spectroscopy to physiological changes and processes.

7. Outlook

In order to substantiate the proposed framework a clinical study containing MR imaging for individual skin layer thickness determination and dielectric measurements is in preparation. A refinement of the unit cell models of the epidermis (shape transition from keratinocyte to corneocyte), dermis and muscle tissue (replacement of unit cells calculated with the HB formula by realistic numerical models) is ongoing. Further optimization of the numerical model, such as incorporation of bound water shells, organelles and ion channels on the microscopic level and hair follicles and sweat glands on the macroscale is also the subject of current work.

Acknowledgments

The authors would like to thank Hansruedi Benedickter, Dirk Baumann and Christoph Böcklin from the Laboratory for Electromagnetic Fields and Microwave Electronics, ETH Zurich for technical assistance during dielectric measurements. Michael Wyss from the Institute for Biomedical Engineering,

ETH Zurich, is thanked for the acquisition of MR images. Mark Talary and Lisa Falco from Solianis Monitoring AG are thanked for scientific discussions.

References

- [1] Walker D C, Brown B H, Smallwood R H, Hose D R and Jones D M 2002 Modelled current distribution in cervical squamous tissue *Physiol. Meas.* **23** 159–68
- [2] Åberg P, Geladi P, Nicander I, Hansson J, Holmgren U and Ollmar S 2005 Non-invasive and microinvasive electrical impedance spectra of skin cancer—a comparison between two techniques *Skin Res. Technol.* **11** 281–6
- [3] Ferreira D M, Silva C S and Souza M N 2007 Electrical impedance model for evaluation of skin irritation in rabbits and humans *Skin Res. Technol.* **13** 259–67
- [4] Marzec E and Warchol W 2005 Dielectric properties of a protein-water system in selected animal tissues *Bioelectrochemistry* **65** 89–94
- [5] Miettinen M, Mönkkönen J, Lahtinen M R, Nuutinen J and Lahtinen T 2006 Measurement of oedema in irritant-exposed skin by a dielectric technique *Skin Res. Technol.* **12** 235–40
- [6] Bagnaninchi P-O, Dikeakos M, Veres T and Tabrizian M 2004 Complex permittivity measurement as a new noninvasive tool for monitoring *in vitro* tissue engineering and cell signature through the detection of cell proliferation,

- differentiation, and pretissue formation *IEEE Trans. Nanobiosci.* **3** 243–50
- [7] Skourou C, Rohr A, Hoopes P J and Paulsen K D 2007 *In vivo* EIS characterization of tumour tissue properties is dominated by excess extracellular fluid *Phys. Med. Biol.* **52** 347–63
- [8] Hakoda M, Hachisu T, Wakizaka Y, Mii S and Kitajima N 2005 Development of a method to analyze single cell activity by using dielectrophoretic levitation *Biotechnol. Prog.* **21** 1748–53
- [9] Yang J, Huang Y, Wang X, Wang X B, Becker F F and Gascoyne P R C 1999 Dielectric properties of human leukocyte subpopulations determined by electrorotation as a cell separation criterion *Biophys. J.* **76** 3307–14
- [10] Morgan H, Sun T, Holmes D, Gawad S and Green N G 2007 Single cell dielectric spectroscopy *J. Phys. D: Appl. Phys.* **40** 61–70
- [11] Debuissson D, Treizebré A, Houssin T, Leclerc E, Bartès-Biesel D, Legrand D, Mazurier J, Arscott S, Bocquet B and Senéz V 2008 Nanoscale devices for online dielectric spectroscopy of biological cells *Physiol. Meas.* **29** S213–25
- [12] Sun T, Gawad S, Green N G and Morgan H 2007 Dielectric spectroscopy of single cells: time domain analysis using Maxwell's mixture equation *J. Appl. Phys. D: Appl. Phys.* **40** 1–8
- [13] Gimsa J, Müller T, Schnelle T and Fuhr G 1996 Dielectric spectroscopy of single human erythrocytes at physiological ionic strength: dispersion of the cytoplasm *Biophys. J.* **71** 495–506
- [14] Talary M S, Dewarrat F, Huber D and Caduff A 2007 *In vivo* life sign application of dielectric spectroscopy and non-invasive glucose monitoring *J. Non-Cryst. Solids* **353** 4515–7
- [15] Martinsen Ø G, Grimnes S and Sveen O 1997 Dielectric properties of some keratinised tissues: I. Stratum corneum and nail *in situ Med. Biol. Eng. Comput.* **35** 172–6
- [16] Alanen E, Lahtinen T and Nuutinen J 1999 Measurement of dielectric properties of subcutaneous fat with open-ended coaxial probes *Phys. Med. Biol.* **43** 475–85
- [17] Naito S, Hoshi M and Yagihara S 1998 Microwave dielectric analysis of human stratum corneum *in vivo Biochim. Biophys. Acta* **1381** 293–304
- [18] Gabriel S, Lau R W and Gabriel C 1996 The dielectric properties of biological tissues: III. Parametric models for the dielectric spectrum of tissues *Phys. Med. Biol.* **41** 2271–93
- [19] Raicu V, Kitagawa N and Irimajiri A 2000 A quantitative approach to the dielectric properties of the skin *Phys. Med. Biol.* **45** L1–4
- [20] Tataru T and Tsuzaki K 2000 Derivation of extracellular fluid volume fraction and equivalent dielectric constant of the cell membrane from dielectric properties of the human body: II. A preliminary study for tracking the progression of surgical tissue injury *Med. Biol. Eng. Comput.* **38** 384–9
- [21] Raicu V, Saibara T and Irimajiri A 1998 Dielectric properties of rat liver *in vivo*: a noninvasive approach using an open-ended coaxial probe at audio/radio frequencies *Bioelectrochem. Bioenergetics* **47** 325–32
- [22] Golombek M-A, Riedel C H and Dössel O 2002 Calculation of the dielectric properties of biological tissue using simple models of cell patches *Biomed. Tech. (Berl)* **47** 253–6
- [23] Peters M J, Hendriks M and Stinstra J G 2001 The passive dc conductivity of human tissues described by cells in solution *Bioelectrochemistry* **53** 155–60
- [24] Huclova S, Erni D and Fröhlich J 2010 Modelling effective dielectric properties of materials containing diverse types of biological cells *J. Phys. D: Appl. Phys.* **43** 365405
- [25] Chrit L, Bastien P, Sockalingum G D, Batisse D, Leroy F, Manfait M and Hadjur C 2006 An *in vivo* randomized study of human skin moisturization by a new confocal raman fiber-optic microprobe: assessment of a glycerol-based hydration cream *Skin Pharmacol. Physiol.* **19** 207–15
- [26] Wertz P W 2005 Stratum corneum lipids and water *Exogenous Dermatol.* **3** 53–6
- [27] Chen L, Lian G and Han L 2008 Use of 'bricks and mortar' model to predict transdermal permeation: model development and initial validation *Ind. Eng. Chem. Res.* **47** 6465–72
- [28] Kashibuchi N, Hirai Y, O'Goshi K and Tagami H 2002 Three-dimensional analyses of individual corneocytes with atomic force microscope; morphological changes related to age, location and to the pathologic skin conditions *Skin Res. Technol.* **8** 203–11
- [29] Potts R O and Francoeur M L 1991 The influence of stratum corneum morphology on water permeability *J. Investigative Dermatol.* **96** 495–99
- [30] Bouwstra J A, de Graaff A, Gooris G S, Nijssse J, Wiechers J W and van Aelst A C 2003 Water distribution and related morphology in human stratum corneum at different hydration levels *J. Investigative Dermatol.* **120** 750–8
- [31] Nakagawa N, Sakai S, Matsumoto M, Yamada K, Nagano M, Yuki T, Sumida Y and Uchiwa H 2004 Relationship between nmf (lactate and potassium) content and the physical properties of the stratum corneum in healthy subjects *J. Investigative Dermatol.* **122** 755–63
- [32] Klein-Szanto A J P 1977 Clear and dark basal keratinocytes in human epidermis *J. Cutaneous Pathol.* **4** 275–80
- [33] Lee A J, King J R and Rogers T G 1996 A multiple-pathway model for the diffusion of drugs in skin *Math. Med. Biol.* **13** 127
- [34] Mogensen M, Morsy H A, Thrane L and Jemec G B E 2008 Morphology and epidermal thickness of normal skin imaged by optical coherence tomography *Dermatology* **217** 14–20
- [35] Prum R O and Torres R H 2004 Structural colouration of mammalian skin: convergent evolution of coherently scattering dermal collagen arrays *J. Exp. Biol.* **207** 2157
- [36] Meglinski I V and Matcher S J 2002 Quantitative assessment of skin layers absorption and skin reflectance spectra simulation in the visible and near-infrared spectral regions *Physiol. Meas.* **23** 741–53
- [37] Tamura T, Tenhunen M, Lahtinen T, Repo T and Schwan H P 1994 Modeling of the dielectric properties of normal and irradiated skin *Phys. Med. Biol.* **39** 927–36
- [38] Novotny G E and Gnoth C 1991 Variability of fibroblast morphology *in vivo*: a silver impregnation study on human digital dermis and subcutis *J. Anatomy* **177** 195–207
- [39] Silver F H, Freeman J W and DeVore D 2001 Viscoelastic properties of human skin and processed dermis *Skin Res. Technol.* **7** 18–23
- [40] Després J P, Savard R, Tremblay A and Bouchard C 1983 Adipocyte diameter and lipolytic activity in marathon runners: relationship with body fatness *Eur. J. Appl. Physiol. Occupational Physiol.* **51** 223–30
- [41] Gomillion C T and Burg K J L 2006 Stem cells and adipose tissue engineering *Biomaterials* **27** 6052–63
- [42] Huclova S, Baumann D, Talary M S and Fröhlich J 2011 Sensitivity and specificity analysis of fringing-field dielectric spectroscopy applied to a multi-layer system modeling human skin *Phys. Med. Biol.* **56** 7777–93
- [43] Misra D K 1987 A quasi-static analysis of open-ended coaxial lines *IEEE Trans. Microw. Theory Tech.* **35** 925–8
- [44] Levine H and Papas C H 1951 Theory of the circular diffraction antenna *J. Appl. Phys.* **22** 29–43
- [45] Grant J P, Clarke R N, Symm G T and Spyrou N M 1989 A critical study of the open-ended coaxial line sensor

- technique for rf and microwave complex permittivity measurements *J. Phys. E: Sci. Instrum.* **22** 757
- [46] Midmore B R, Hunter R J and O'Brien R W 1987 The dielectric response of concentrated lattices *J. Colloid Interface Sci.* **120** 210–7
- [47] Gabriel C 2006 Dielectric properties of biological materials *Handbook of Biological Effects of Electromagnetic Fields* (London: Taylor and Francis) pp 52–94
- [48] Smith S R and Foster K R 1985 Dielectric properties of low-water-content tissues *Phys. Med. Biol.* **30** 965–73
- [49] Sihvola A H 1999 *Electromagnetic Mixing Formulas and Applications* (London, UK: INSPEC/IEE)
- [50] Bai W, Zhao K S and Asami K 2006 Dielectric properties of *E. coli* cell as simulated by the three-shell spheroidal model *Biophys. Chem.* **122** 136–42
- [51] Sebastián J L, Muñoz S, Sancho M, Álvarez G and Miranda J M 2007 Electric field distribution and energy absorption in anisotropic and dispersive red blood cells *Phys. Med. Biol.* **52** 6831–47
- [52] Raicu V, Saibara T, Enzan H and Irimajiri A 1998 Dielectric properties of rat liver *in vivo*: analysis by modeling hepatocytes in the tissue architecture *Bioelectrochem. Bioenergetics* **47** 333–42
- [53] Sihvola A and Lindell I V 1990 Polarizability and effective permittivity of layered and continuously inhomogeneous dielectric ellipsoids *J. Electromagn. Waves Appl.* **4** 1–26
- [54] Simeonova M, Wachner D and Gimsa J 2002 Cellular absorption of electric field energy: influence of molecular properties of the cytoplasm *Bioelectrochemistry* **56** 215–8
- [55] Kretsos K and Kasting G B 2007 A geometrical model of dermal capillary clearance *Math. Biosci.* **208** 430–53
- [56] Vitellarq-Zuccarello L, Dyne K and Cetta G 1989 Biochemical, morphological and stereological study of the dermis in three members of a large family with type iv ehlers-danlos syndrome *Connective Tissue Res.* **23** 1–17
- [57] Asami K 2002 Characterization of heterogeneous systems by dielectric spectroscopy *Prog. Polym. Sci.* **27** 1617–59
- [58] Donev A, Cisse I, Sachs D, Variano E A, Stillinger F H, Connelly R, Torquato S and Chaikin P M 2004 Improving the density of jammed disordered packings using ellipsoids *Science* **303** 990–3
- [59] Gheorghiu E, Balut C and Gheorghiu M 2002 Dielectric behaviour of gap junction connected cells: a microscopic approach *Phys. Med. Biol.* **47** 341–8
- [60] Lei J, Wan J T K, Yu K W and Sun H 2001 First-principle approach to dielectric behaviour of nonspherical cell suspensions *Phys. Rev. E* **64** 012903
- [61] Gielis J 2003 A generic geometric transformation that unifies a wide range of natural and abstract shapes *Am. J. Botany* **90** 333–8
- [62] Frasch H F and Barbero A M 2003 Steady-state flux and lag time in the stratum corneum lipid pathway: results from finite element models *J. Pharmaceutical Sci.* **92** 2196–207
- [63] Alanen E, Lahtinen T and Nuutinen J 1999 Penetration of electromagnetic fields of an open-ended coaxial probe between 1 MHz and 1 GHz in dielectric skin measurements *Phys. Med. Biol.* **44** N169–76
- [64] Cowen J A, Imhof R E and Xiao P 2001 Opto-thermal measurement of stratum corneum renewal time *Anal. Sci.* **17** 353–6
- [65] Egawa M, Hirao T and Takahashi M 2007 *In vivo* estimation of stratum corneum thickness from water concentration profiles obtained with raman spectroscopy *Acta Dermato-Venerologica* **87** 4–8
- [66] Moore T L, Lunt M, McManus B, Anderson M E and Herrick A L 2003 Seventeen-point dermal ultrasound scoring system—a reliable measure of skin thickness in patients with systemic sclerosis *Rheumatology* **42** 1559–63
- [67] Miklavčič D, Pavšelj N and Hart F X 2006 Electric properties of tissues *Wiley Encyclopedia of Biomedical Engineering* (New York: Wiley) pp 1–12
- [68] Yamamoto T and Yamamoto Y 1976 Electrical properties of the epidermal stratum corneum *Med. Biol. Eng.* **14** 151–8
- [69] Mäurer J, Requardt H, Sander B, Knollmann F D, Lemke A-J, Vogl T J and Felix R 1996 Applications of specialized coils for high-resolution MRI on a whole-body scanner *Mag. Resonance Mater. Phys. Biol. Med.* **4** 27–33
- [70] Gabriel C, Gabriel S and Corhout E 1996 The dielectric properties of biological tissues: I. Literature survey *Phys. Med. Biol.* **41** 2231–49